buildings

MDPI

Article

Seismic Performance of Precast Concrete Bridge Piers with Built-In Steel Tube Connection Key

Renwei Zhang [1,2], Liqun Zheng [3], Hai Zhong [1,4,*] and Shuangshuang Qin [1,4]

[1] School of Civil Engineering, Sanming University, Sanming 365004, China; 20080620@fjsmu.edu.cn (R.Z.); 20180132@fjsmu.edu.cn (S.Q.)
[2] Key Laboratory of Intelligent Construction and Monitoring of Engineering Structures in Fujian Province College, Sanming 365004, China
[3] Fujian No.1 Construction Group Co., Ltd., Sanming 365001, China; 20151100@fjsmu.edu.cn
[4] Key Laboratory of Engineering Material & Structure Reinforcement in Fujian Province College, Sanming 365004, China
* Correspondence: hzhong@fjsmu.edu.cn

Abstract: Investigating the seismic behavior of precast concrete bridge piers is crucial in the design process due to the complex stress distribution in the connecting components. To demonstrate the seismic behavior of precast concrete bridge piers with hybrid joint connections, three bridge piers were designed with a scaling ratio of 1:8 and then tested under low cyclic loading conditions. The tests involved varying shapes of steel tube connection keys as parameters. This study involved examining failure modes and crack development, as well as analyzing the hysteretic performance, deformation capacity, energy dissipation, and stiffness degradation of the specimens. Furthermore, a finite element model was developed using ABAQUS, and the validity of the modeling approach suggested in this study was confirmed through tests. The results indicate that the precast piers exhibit reduced concrete damage at the joints. The enhanced strength of the joints is attributed to the incorporation of steel tube connection keys. The circular steel tube connection key integrated into the precast bridge pier offers a superior bearing capacity, energy dissipation, and stiffness degradation compared to the cross-shaped steel tube connection key. The presence of the built-in circular steel tube connection key in the precast bridge pier suggests that it complies with the seismic structural measures and is consistent with the design principle of "strong joint and weak member".

Keywords: bridge engineering; precast pier; steel tube connector key; hybrid joint; quasi-static test; hysteretic characteristics; finite element modeling

Citation: Zhang, R.; Zheng, L.; Zhong, H.; Qin, S. Seismic Performance of Precast Concrete Bridge Piers with Built-In Steel Tube Connection Key. *Buildings* **2024**, *14*, 3470. https://doi.org/10.3390/buildings14113470

Received: 11 September 2024
Revised: 18 October 2024
Accepted: 28 October 2024
Published: 30 October 2024

1. Introduction

Precast concrete bridge piers exhibit a short construction period, environmentally friendly characteristics, controllable quality, and minimal impact on existing traffic [1]. They align with the principles of "green construction" and are extensively employed in constructing cross-sea bridges, urban viaducts, and other bridge structures [2–4]. Common projects encompass the Lake Pontchartrain Bridge (USA) [5], East Sea Bridge (China) [6], and Hong Kong–Zhuhai–Macao Bridge (China) [7]. Concurrently, the typical connection methods for precast concrete bridge piers encompass grouting sleeve connection [8,9], grouted corrugated steel sleeve connection [10], socket connection [11], prestressed connection [12], and wet joint connection [13]. Among these, the grouting sleeve is the most commonly utilized connection method in precast concrete bridge piers [14]. However, the use of grouting sleeves to connect piers in practical engineering applications is predominantly observed in low seismic areas, with limited application in medium and high seismic areas [15]. Therefore, further research is necessary to investigate the seismic behavior of the precast concrete bridge piers.

In recent years, researchers have conducted experimental studies, theoretical discussions, and finite element analyses on precast concrete bridge piers connected through grouting sleeves. Zou et al. [16] carried out full-scale tests on precast assembled bridge piers (PABPs) with hybrid connection using both tendons and socket connections and then established an elastic–plastic fiber model of PABPs by using finite element software (OpenSees). The study shows that the prestressing tendons and socket connection can provide enough ductility, strength, recovery capacity, and bending strength under small horizontal displacements. Increasing prestress force can improve the bearing capacity and post-yield stiffness of the pier to a certain extent, but the ductility decreases and the residual deformation increases. Wang et al. [17] examined the impact of column height on the seismic behavior of grouted splice piers. The findings indicated that the ultimate lateral force of grouted splice piers underwent an approximate 10% increase. Xin et al. [18] demonstrated that concrete piers interconnected through a combination of grouting sleeves and prestressing tendons exhibit enhanced load-carrying capacity, ductility, and energy dissipation. They also introduced a methodology for determining the horizontal load-carrying capacity. Wang et al. [19] developed a plastic hinge model that is equivalent to precast piers connected by sleeves. This model considers the influences of bending, shear, longitudinal reinforcement slip, and casing length. Liu et al. [20] analyzed the impact of grouting sleeve location on the seismic behavior of precast bridge piers. The findings indicated a reduction in ductility and energy consumption in piers connected with grouting sleeves at the end of columns and at the bottom of bent caps. As a result, it is not advisable to utilize this type of connection in high-intensity areas. Wang et al. [21] conducted quasi-static cyclic tests on precast piers. The results indicated that incorporating shear keys or altering the bond material contributed to enhancing the structural integrity. However, it was not readily apparent that these measures improved the seismic behavior of precast piers. In addition, Kenarkoohi et al. [22] provide a comprehensive discussion of prefabricated elements systems, describing their applicability, advantages, and limitations. Qu et al. [23] performed shaking table experiments on precast piers linked by grouted splice sleeve couplers and investigated finite element modeling techniques employing OpenSEES. Subsequently, Ding et al. [24], Lei et al. [25], and Li et al. [26] constructed a finite element model for precast concrete bridge columns with grouted sleeve connections, which was then calibrated using test results. Additionally, Huang et al. [27] conducted a finite element analysis on precast beam–column connection components using ABAQUS, validating the effectiveness of their finite element modeling approach through tests. Currently, various modeling methods have been proposed for different components, but the applicability of these existing methods to precast concrete bridge piers still requires further investigation.

In light of the limitations associated with the conventional connection method, including the single force transfer mode, inadequate shear strength at the connection, and challenges in ensuring grouting quality, this study introduces a steel tube connection key at the grouting sleeve connection. It is anticipated that this innovation will significantly enhance the connection capacity at the junction of the precast concrete bridge pier. Consequently, three specimens were prefabricated to elucidate the seismic behavior of precast concrete bridge piers with integrated steel tube connection keys through the implementation of the suggested quasi-static tests. A refined modeling method for precast concrete bridge piers is proposed on this basis, and the research findings offer theoretical direction and technical assistance for engineering applications.

2. Experimental Program

2.1. Specimen Design

To investigate the seismic behavior of precast concrete bridge piers connected by hybrid joints, three different types of pier structures were designed at a scale ratio of 1:8. The specific configurations of the specimens are depicted in Figure 1. The pier has an effective height of 1100 mm and a pier body diameter of 250 mm. The loading end of the specimen measures 360 mm × 360 mm × 200 mm, while the ground beam measures

800 mm × 800 mm × 500 mm. The cast-in-place concrete pier (CIP specimen) features a pier shaft that is uniformly equipped with 8 longitudinal bars of HRB400 grade, each with a 12 mm diameter, arranged along the circumferential direction. Additionally, the stirrups are densely positioned in the plastic hinge area. The cross-sectional view of the CIP specimen is depicted in Figure 1a. The precast concrete bridge pier with a built-in circular steel tube connecting key (GY specimen) is equipped with 8 grouting sleeves arranged along the circumferential direction at the joint. The circular steel tube connecting key, with a diameter of 100 mm and a thickness of 8 mm, is positioned at the center of the joint. The connecting length of the steel tube connecting key is determined to be 200 mm in accordance with the specifications outlined in the GB 50936-2014 code [28]. The cross-sectional view of the GY specimen is depicted in Figure 1b. Furthermore, the precast concrete bridge pier with integrated cross-shaped steel tube connection keys (GS specimen) exhibits a similar cross-sectional configuration to the GY specimen, as shown in Figure 1c.

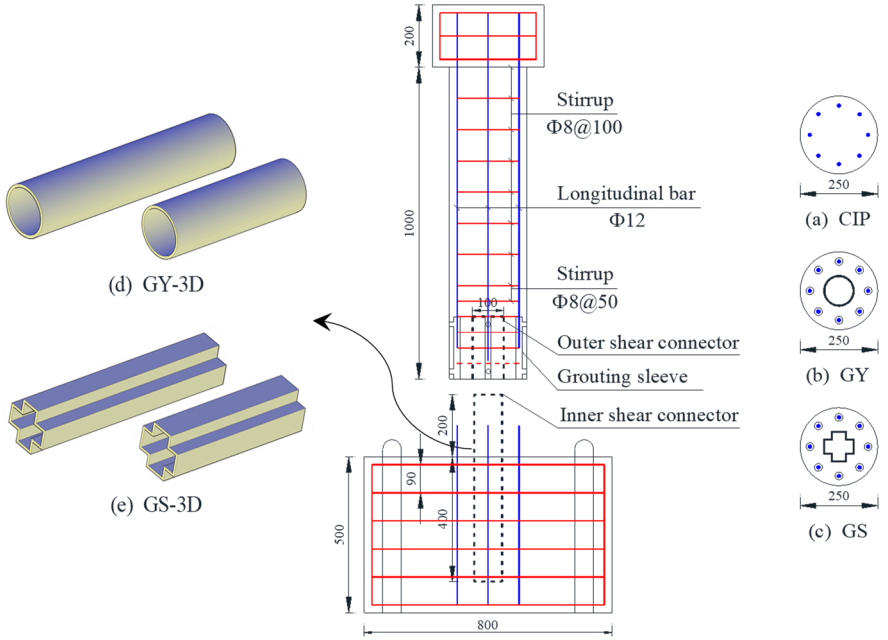

Figure 1. Specimen details (unit: mm).

Figure 2 illustrates the manufacturing process of specimens. To guarantee the complete filling of the grouting sleeve with grout, pressure is applied from the lower end of the sleeve during the filling process until the grout is expelled from the grouting port on the upper side, at which point the pressure application is halted.

(**a**) (**b**) (**c**)

Figure 2. *Cont.*

(**d**) (**e**) (**f**)

Figure 2. Manufacturing process of specimens. (**a**) Strain gauge sticking; (**b**) reinforcement cage; (**c**) shear connector; (**d**) surface cleaning; (**e**) pier shaft; (**f**) grouting.

2.2. Material Properties

The concrete utilized in this test has a strength grade of C40, and cubic concrete blocks are set aside for the pouring of specimens, with curing being conducted under identical conditions to those of the specimens. In accordance with the GB/T 50081-2019 standard [29], the results of the measurable physical characteristics of concrete are displayed in Table 1. The high-strength, non-shrinkage grouting material is produced by Beijing Sida Jianmao Technology Development Co., Ltd. (Beijing, China) Furthermore, three sets of 100 mm × 100 mm × 100 mm mortar blocks were set aside during the grouting with the grouting sleeve, and the compressive strength of the mortar blocks was determined to be 101.2 MPa.

Table 1. Mechanical indexes of C40.

Grade of Concrete	Cubic Compressive Strength (MPa)	Prism Compressive Strength (MPa)	Modulus of Elasticity (GPa)
C40	42.8	29.1	32.4

The steel strength grade is Q235. According to the specification requirements of GB/T 228.11-2010 [30], the measured yield strength is 309.5 MPa, the tensile strength is 429.7 MPa, and the modulus of elasticity is 2.0×10^5 MPa. The reinforcing bars have a strength grade of HRB400, and material property tests for 8 mm and 12 mm reinforcing bars are performed during the processing of the reinforcement cage. Based on the GB/T 228.11-2010 specification, the performance indexes of the reinforcing bars are presented in Table 2.

Table 2. Performance indexes of reinforcing bars.

Grade of Reinforcing Bars	Bar Diameter (mm)	Yield Strength (MPa)	Ultimate Strength (MPa)	Elongation (%)
HRB400	8	419	601	30.9
HRB400	12	478	622	28.2

2.3. Test Setup and Measurement

The specimen had an axial compression ratio of 0.2, and the test loading device is depicted in Figure 3. A vertical hydraulic jack with a vertical range of 100 tons was employed for the test loading. The horizontal actuator is a 100-ton MTS hydraulic servo actuator capable of exerting a maximum horizontal displacement of 250 mm. To prevent specimen slippage, the bearing platform was installed with two jacks in the horizontal direction. To

monitor the displacement across the length of the specimen, three linear variable differential transformers (LVDTs) were placed on both the left and right sides of the pier, with vertical LVDTs set at a distance of 150 mm. Additionally, reinforcement and concrete strain gauges were installed in the plastic hinge region to monitor the strain distribution.

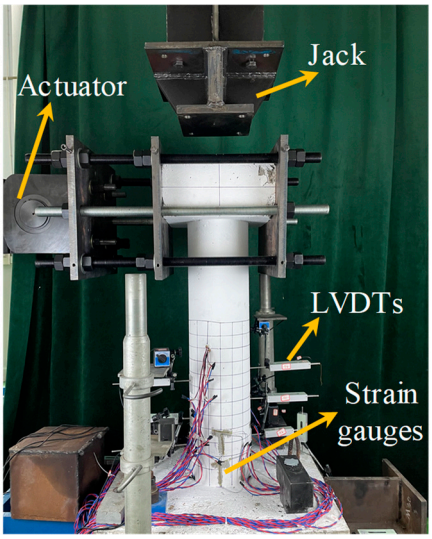

Figure 3. Schematics of test loading device.

2.4. Loading System

In accordance with GB50011–2010 [31], displacement-controlled loading is employed for the specimen, with three cycles at each displacement level. The test is completed when the horizontal load-bearing capacity of the specimen is decreased to 85% of its maximum load-bearing capacity. The loading protocol is depicted in Figure 4.

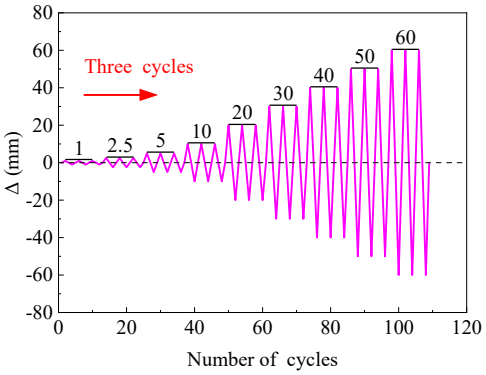

Figure 4. Loading protocol.

3. Results and Discussion

3.1. Failure Modes

The failure modes of each specimen are depicted in Figure 5. As shown in Figure 5a, the CIP specimen exhibits no discernible alteration during the elastic stage. Upon reaching a displacement of 2.5 mm, the CIP specimen exhibits the initiation of fine cracks at the root position. As displacement increases, the reinforcing bars yield first, leading to the formation of a plastic hinge at the end of the pier. Upon reaching a displacement of 30 mm, a decline in strength and stiffness is observed, attributed to the presence of a circumferential crack in the CIP specimen located approximately 50 mm from the ground beam. Subsequently, the concrete cover on the push–pull side of the CIP specimen within 100 mm from the ground beam exhibits notable spalling, leading to substantial residual displacement and a significant reduction in both bearing capacity and recoverability.

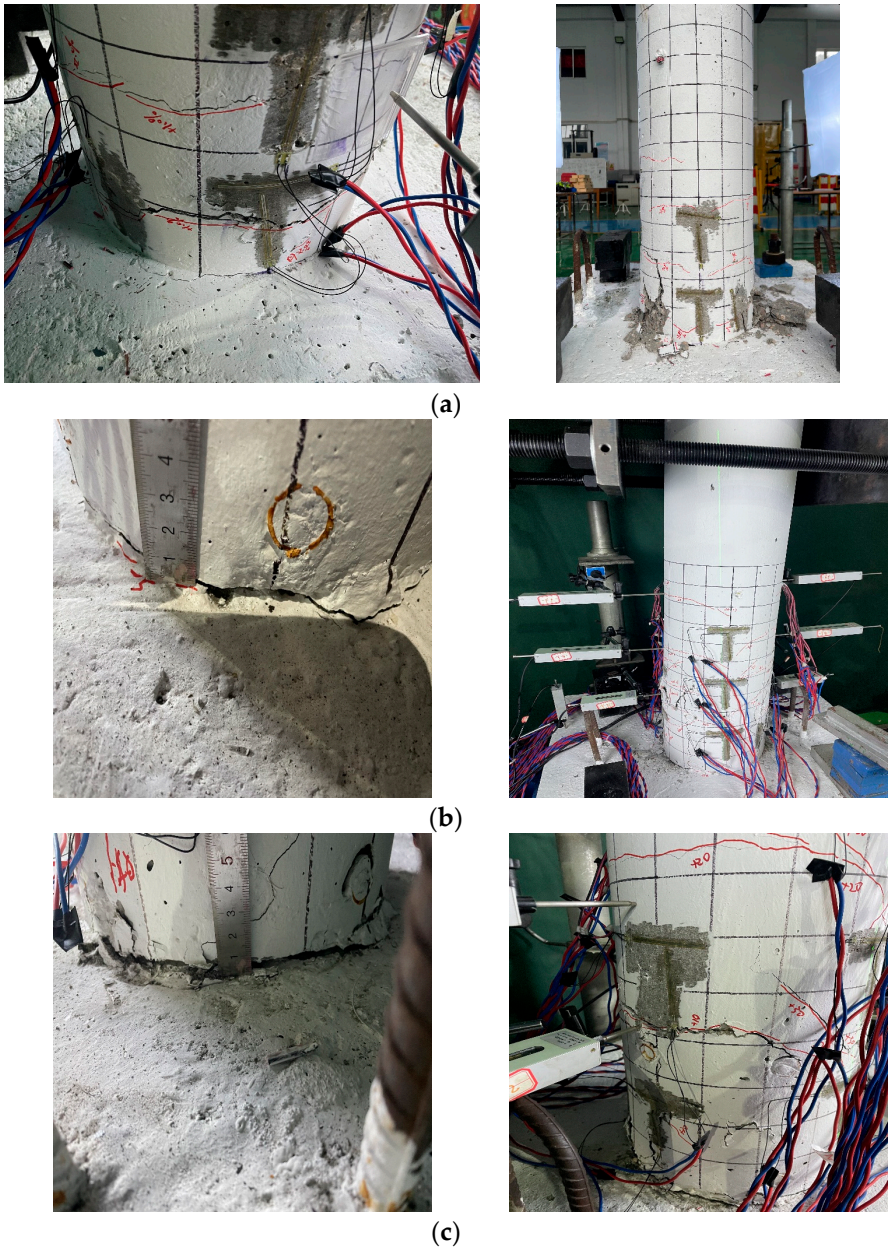

Figure 5. Comparative analysis of failure patterns in specimens. (**a**) CIP specimen; (**b**) GY specimen; (**c**) GS specimen.

The GY specimen exhibits similar characteristics to the CIP specimen during the initial stage, with all materials in an elastic state and no discernible changes on the outer surface of the specimen. Upon reaching a horizontal displacement of 5 mm, small cracks start to appear on the GY specimen located on the upper side of the sleeve. When a 10 mm horizontal displacement is applied, the pier shaft gradually lifts on the pulling side, reaching a height of approximately 3 mm. As the horizontal displacement continues to increase, the specimen begins to show a gradual emergence of cracks in both the horizontal and vertical directions within a distance of 500 mm from the ground beam. Upon applying a horizontal displacement of 30 mm, a conspicuous circumferential crack emerges on the upper side of the sleeve, as depicted in Figure 5b. Subsequently, the cracks on the upper side of the sleeve progressively expand, resulting in a continuous reduction in the bearing capacity and ultimately leading to the bending failure of the GY specimen. The damage process of the GS specimen exhibits similarities to that of the GY specimen. However, the pier is progressively raised to a greater height of approximately 7 mm on the pull

side. This phenomenon could be ascribed to the presence of certain slippage between the cross-shaped steel tubes during the pushing and pulling process of the specimen, as well as to the impact of machining accuracy. Figure 5c illustrates the ultimate failure of the GS specimen.

In comparison to CIP specimen, the damage to the precast concrete bridge pier (GS and GY specimens) within 200 mm of the ground beam is reduced. The predominant damage location is on the upper side of the sleeves, attributed to the inclusion of the steel tube connection key at the joint. This addition notably enhances the joint strength, leading to an upward shift in the plastic hinge region in the precast concrete bridge piers. After the test, the concrete in the plastic hinge region is removed by chiseling, revealing the internal reinforcing bar, grouting sleeve, and steel tube connection key, as depicted in Figure 6. This figure illustrates that the chiseling results in more significant deformation of the reinforcing bar, while the sleeve and the steel tube connection key do not exhibit significant damage, suggesting the feasibility of the built-in steel tube connection key scheme for reinforcing the splice of the precast concrete bridge pier.

(**a**) (**b**)

Figure 6. Failure modes in components. (**a**) Reinforcing bars; (**b**) grouting sleeves.

3.2. Hysteretic Response

The horizontal load–displacement (P-Δ) hysteretic curves of the specimens are shown in Figure 7. These show that the load and displacement are positive when the load is positive, and they are negative when the load is negative.

In the early stage of loading, the materials are in a state of elastic deformation, and the hysteretic curve shows a linear response. As the horizontal displacement increases, the hysteretic curve's area expands, leading to a gradual enhancement of the specimen's energy dissipation capacity. As the reinforcing bar undergoes yielding, the specimen progressively transitions into the elastic–plastic stage, leading to a corresponding decrease in stiffness. Owing to the minor slippage between the reinforcement and concrete, as well as the inner and outer steel tubes during the push–pull process of the specimen, the hysteretic curves of the specimens exhibit a certain pinching phenomenon, resulting in a bow-shaped curve, as depicted in Figure 7. Furthermore, the hysteretic curves of the precast concrete bridge piers with built-in steel tube connecting keys exhibit pronounced asymmetry in both the positive and negative directions. This can be attributed to factors such as the vertical jack not being located at the center of the specimen, inadequate machining accuracy of the specimens, and the greater friction force exerted by the MTS horizontal actuator, but the hysteretic curves exhibit a greater fullness and demonstrate a strong capacity for energy dissipation.

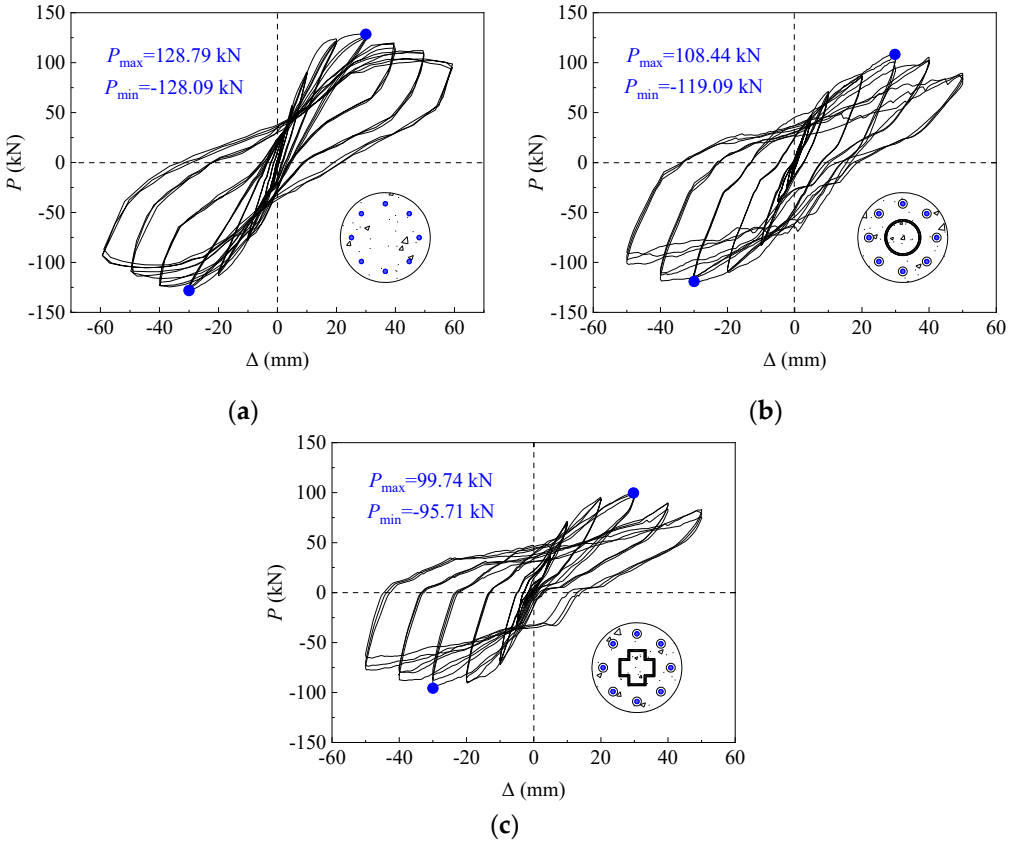

Figure 7. Hysteretic curves of specimens. (**a**) CIP specimen; (**b**) GY specimen; (**c**) GS specimen.

3.3. Skeleton Curves and Ductility

The skeleton curves were derived from the peak points of the initial loading cycle across all levels of the load–displacement hysteretic curves, as illustrated in Figure 8. The specimen's yield point was determined using the calculation guidelines outlined in Figure 9. The specific parameters of the specimen can be found in Table 3. The displacement ductility coefficient (μ) represents the ultimate displacement (Δ_u) to the yield displacement (Δ_y) [32], which is given as follows:

$$\mu = \frac{\Delta_u}{\Delta_y} \quad (1)$$

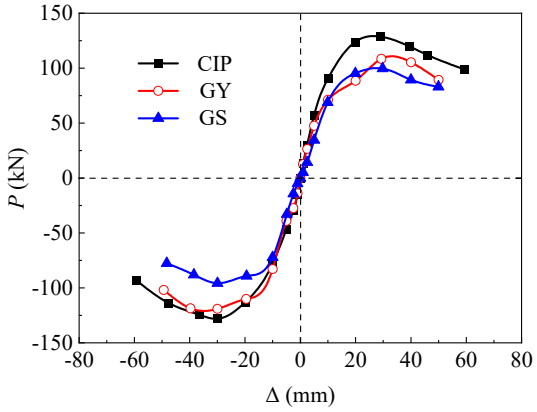

Figure 8. Skeleton curves of specimens.

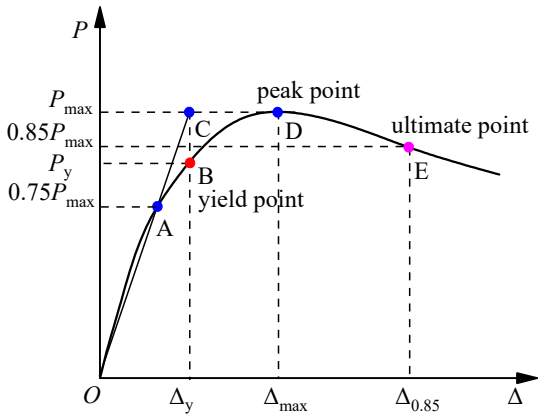

Figure 9. Equivalent elastoplastic energy analysis method.

Table 3. Feature points from specimen skeleton curves.

Specimens	Loading Direction	P_y (kN)	Δ_y (mm)	P_{max} (kN)	Δ_{max} (mm)	P_u (kN)	Δ_u (mm)	μ
CIP	Positive	114.92	14.35	128.79	28.85	109.47	47.87	3.34
	Negative	109.61	18.26	128.09	30.00	108.87	51.08	2.80
	Average	112.27	16.31	128.44	29.43	109.17	49.48	3.07
GY	Positive	88.46	17.83	108.44	29.28	92.17	48.23	2.71
	Negative	103.11	15.12	119.09	29.97	101.23	49.79	3.29
	Average	95.79	16.48	113.77	29.63	96.70	49.01	3.00
GS	Positive	86.11	15.92	99.74	29.74	84.78	47.54	2.99
	Negative	84.94	15.32	95.71	29.97	81.35	45.92	3.00
	Average	85.53	15.62	97.73	29.86	83.07	46.73	3.00

As depicted in Figure 8, the skeletal curves of the specimens exhibit an S-shaped pattern, suggesting that the specimens primarily undergo elastic, elastic–plastic, and failure stages during the loading process. During the initial loading stage, the skeleton curves exhibit greater coincidence in the elastic phase. However, as displacement gradually increases, the precast concrete bridge piers enter the elastic–plastic stage at an earlier point.

According to Table 3 (where the average analysis is conducted for the positive and negative values to facilitate data observation), the load-bearing capacity of the GY and GS specimens decreased by 11.4% and 23.9%, respectively, in comparison to the CIP specimen. The load bearing-capacity of the GY specimen increased by approximately 16.4% compared to the GS specimen, indicating that the precast concrete bridge pier with a built-in circular steel tube connection key exhibits a superior load-bearing capacity. Furthermore, Table 3 illustrates that the displacement ductility coefficient of the precast concrete bridge piers is comparable to that of the CIP specimen, both approximately 3.00. This suggests that the built-in steel tube connection key can enhance the deformation capacity of the precast concrete bridge piers.

3.4. Bearing Capacity Degradation

The term "bearing capacity degradation" pertains to the performance of a specimen during cyclic loading [33]. The term refers to the comparison between the maximum horizontal bearing capacity (P_i) at the i-th cycle for each level of loading and the maximum horizontal bearing capacity ($P_{i\text{-}1}$) at the i-1 cycle for the same level of loading. This ratio is represented by the bearing capacity degradation coefficient as follows:

$$\alpha_i = \frac{P_i}{P_{i\text{-}1}} \quad (2)$$

The degradation curves for the bearing capacity of the specimens are calculated using Equation (2), as depicted in Figure 10. The figure illustrates that during the initial loading stage, the bearing capacity degradation coefficient of the specimens fluctuates notably in the negative direction, while it is more consistent in the positive direction. The divergence in strength between the specimens in the positive and negative directions can be explained by the initial defects present in them. Nonetheless, the degradation coefficient of the bearing capacity hovers around 1 with minor fluctuations, indicating that the bearing capacity degradation stays relatively constant.

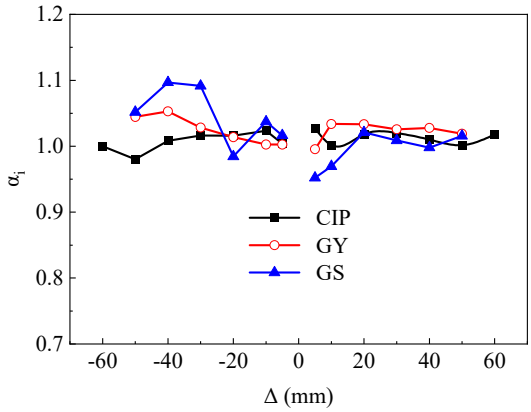

Figure 10. Bearing capacity degradation curves of specimens.

3.5. Energy Dissipation

The region bounded by the hysteretic curve can serve as a representation of the energy dissipated by the specimen during the loading process, and the total energy dissipation (E_S) of the specimen can be determined by integrating the curve at each stage [34], which is calculated as shown in Equation (3). Figure 11 illustrates the variation in E_S with the loading level.

$$E_s = \sum_{i=1}^{x} \Delta W_i \tag{3}$$

where x is the total number of loading levels; and ΔW_i is the hysteretic dissipation energy of the i-th displacement level.

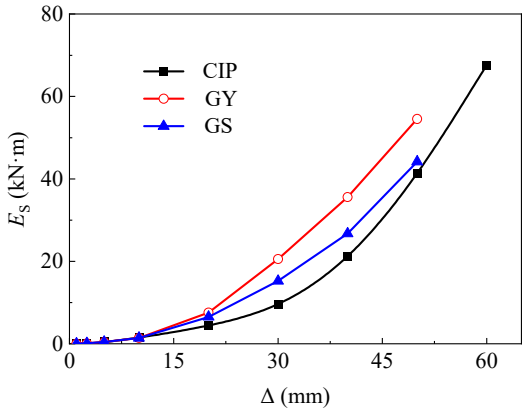

Figure 11. Cumulative hysteretic dissipated energy curves of specimens.

At the beginning of loading, E_S values of the specimens are minimal and the curves exhibit substantial overlap, as depicted in Figure 11. As the horizontal displacement increases, E_S values of the specimens also gradually increase. After the horizontal displacement exceeds 10 mm, E_S of the GY specimen gradually surpasses that of the GS and CIP specimens. Ultimately, E_S of the GY specimen increases by approximately 19.0% compared to that of

the GS specimen. This indicates that by including the circular steel tube connection key at the joint, it is possible to enhance the bending capacity of the specimen and in turn improve the deformation and energy dissipation capacity of the precast concrete bridge pier. Furthermore, as the horizontal displacement reaches 50 mm, the loading of the precast concrete bridge pier stops due to the increased visibility of cracks and yielding of reinforcing bars above the sleeves, as well as a significant decrease in bearing capacity. Meanwhile, the ultimate E_S of the CIP specimen exceeds that of the precast concrete bridge piers due to its superior overall performance.

3.6. Stiffness Degradation

With the rising loading level, the specimen's stiffness will decrease progressively due to the accumulation of damage. The secant stiffness (K_i) is employed to characterize the stiffness reduction of the pier [35]. The calculation formula is represented by Equation (4), and the outcomes of the calculations are depicted in Figure 12. Table 4 displays the stiffness eigenvalues of the specimens, including the average values of both positive and negative eigenvalues.

$$K_i = \frac{|+F_i| + |-F_i|}{|+X_i| + |-X_i|} \tag{4}$$

where $+F_i$ and $-F_i$ are the load values at the positive and negative peak points of the i-th cycle, respectively; and $+X_i$ and $-X_i$ are the displacement values at the positive and negative peak points of the i-th cycle, respectively.

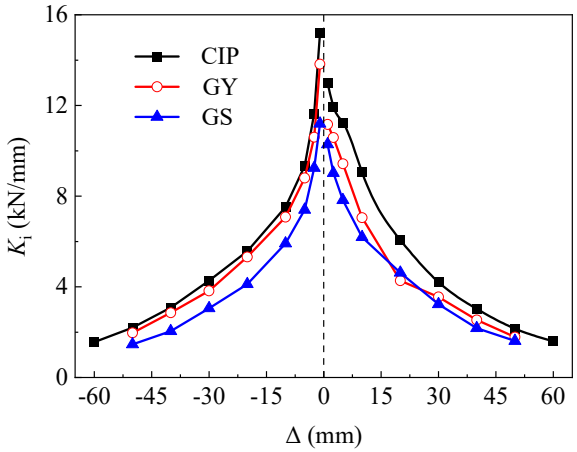

Figure 12. Stiffness degradation curves of specimens.

Table 4. Stiffness eigenvalues of specimens.

Specimens	Initial Stiffness (kN/mm)	Final Stiffness (kN/mm)	Stiffness Degradation Rate (%)
CIP	14.10	1.58	88.8
GY	12.49	1.88	85.0
GS	10.74	1.49	86.1

In the early phase of loading, the stiffness degradation curves show a faster decrease, resulting in a more pronounced stiffness degradation of the specimens, as shown in Figure 12. As displacement increases, the specimens exhibit a tendency for stiffness degradation to plateau. Table 4 illustrates that the CIP specimen exhibits the highest initial stiffness, while the GS specimen demonstrates the lowest, with a decrease of 23.8%. The GY specimen's initial stiffness is comparable to that of CIP specimen, with only an 11.4% reduction. The error falls within the controllable range, suggesting that the incorporation

of a circular steel tube connection key at the splice location of the precast concrete bridge pier is a more rational approach. However, the ultimate rates of stiffness degradation in the specimens are nearly identical, both reaching 85%.

4. Finite Element Modeling

4.1. Stress–Strain Relationships for Construction Materials

4.1.1. Concrete

The concrete constitutive model utilizes the concrete constitutive relationship outlined in Appendix C of the GB 50010-2010 Code [36]. Figure 13 illustrates the uniaxial stress–strain curve. The equations representing the constitutive relationship for concrete compression are given as follows:

$$\sigma = (1 - d_c)E_c\varepsilon \tag{5}$$

$$d_c = \begin{cases} 1 - \frac{\rho_c n}{n - 1 + x^n} & x \le 1 \\ 1 - \frac{\rho_c}{\alpha_c(x-1)^2 + x} & x > 1 \end{cases} \tag{6}$$

$$\rho_c = \frac{f_{c,r}}{E_c\varepsilon_{c,r}} \tag{7}$$

$$n = \frac{E_c\varepsilon_{c,r}}{E_c\varepsilon_{c,r} - f_{c,r}} \tag{8}$$

$$x = \frac{\varepsilon}{\varepsilon_{c,r}} \tag{9}$$

where d_c is the compressive damage evolution parameter of concrete; α_c is the parameter value of the descending section of the concrete's compressive stress–strain curve; $f_{c,r}$ is the representative value of the concrete's compressive strength; and $\varepsilon_{c,r}$ is the concrete's peak compressive strain corresponding to the compressive strength $f_{c,r}$.

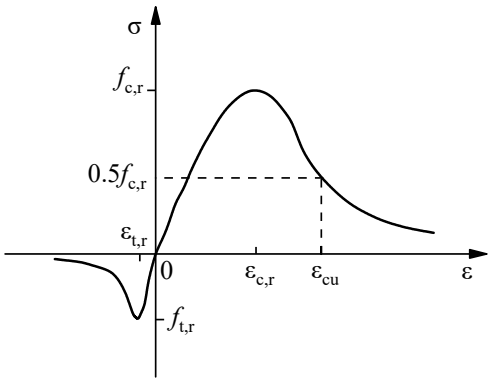

Figure 13. Uniaxial stress–strain curve of concrete.

Additionally, the concrete's uniaxial tensile stress–strain relationship can be expressed as follows:

$$\sigma = (1 - d_t)E_c\varepsilon \tag{10}$$

$$d_t = \begin{cases} 1 - \rho_t\left[1.2 - 0.2x^5\right] & x \le 1 \\ 1 - \frac{\rho_t}{\alpha_t(x-1)^{1.7} + x} & x > 1 \end{cases} \tag{11}$$

$$x = \frac{\varepsilon}{\varepsilon_{t,r}} \tag{12}$$

$$\rho_t = \frac{f_{t,r}}{E_c\varepsilon_{t,r}} \tag{13}$$

where d_t is the uniaxial tensile damage evolution parameter of concrete; α_t is the parameter value of the descending section of the concrete's uniaxial tensile stress–strain curve; $f_{t,r}$ is the representative value of the concrete's uniaxial tensile strength; and $\varepsilon_{t,r}$ is the concrete's peak tensile strain corresponding to the uniaxial tensile strength $f_{t,r}$.

4.1.2. Reinforcing Bar

Menegotto [37] introduced the Giuffre–Menegotto–Pinto model for reinforcing bar hysteresis constitutive performance. This model is characterized by an explicit strain-dependent function, offering straightforward computation, high precision, and the ability to replicate the Bauschinger effect. It has been extensively utilized in the seismic response analysis of reinforced concrete structures. Consequently, the Giuffre–Menegotto–Pinto model was utilized in this study.

4.1.3. Steel Tube

Steel is considered to be a homogeneous ideal material, and the ideal elastoplastic model is applied to the steel tube [38]. The corresponding expression is presented in Equation (14), and the stress–strain curve of the steel is depicted in Figure 14.

$$\sigma_s = \begin{cases} E_s\varepsilon_s & \varepsilon_s \le \varepsilon_y \\ f_y & \varepsilon_s > \varepsilon_y \end{cases} \tag{14}$$

where σ_s is the steel stress; E_s is the steel modulus of elasticity; ε_s is the steel strain; ε_y is the steel yield strain; and f_y is the steel yield strength.

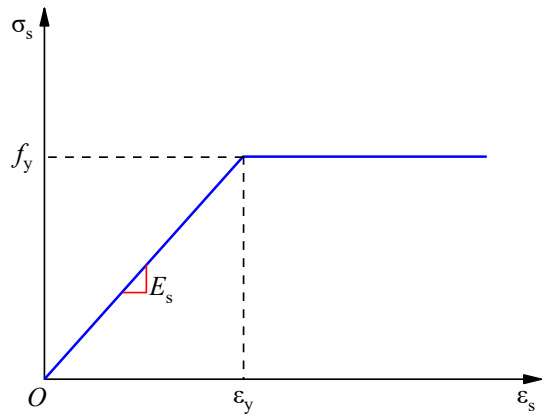

Figure 14. Stress–strain relationship curve of steel tube.

4.2. Modeling and Meshing

The specimens' finite element model was created with the ABAQUS software (ver. 6.14-4). Concrete was represented using C3D8R elements, reinforcing bars using Truss (T3D2) elements, and steel using shell (S4R) elements. Figure 15a illustrates the boundary conditions of the pier in the context of finite element analysis. In consideration of the calculation efficiency and accuracy, the meshing of the components is illustrated in Figure 15a–f. This includes 640 elements for concrete, 320 elements for the grouting sleeve, 944 elements for reinforcing bars, and 176 elements for the steel tube connection keys.

The concrete damage plasticity model was employed in this study for its computational simplicity and convergence in ABAQUS. The control parameters encompass the expansion angle (ψ), eccentricity (ε), the ratio of biaxial to uniaxial ultimate compressive strength (f_{b0}/f_{c0}), the projection shape parameter (K) of the control concrete yield surface on the eccentric plane, and the viscosity coefficient (ω). Table 5 presents the specific values of the parameters.

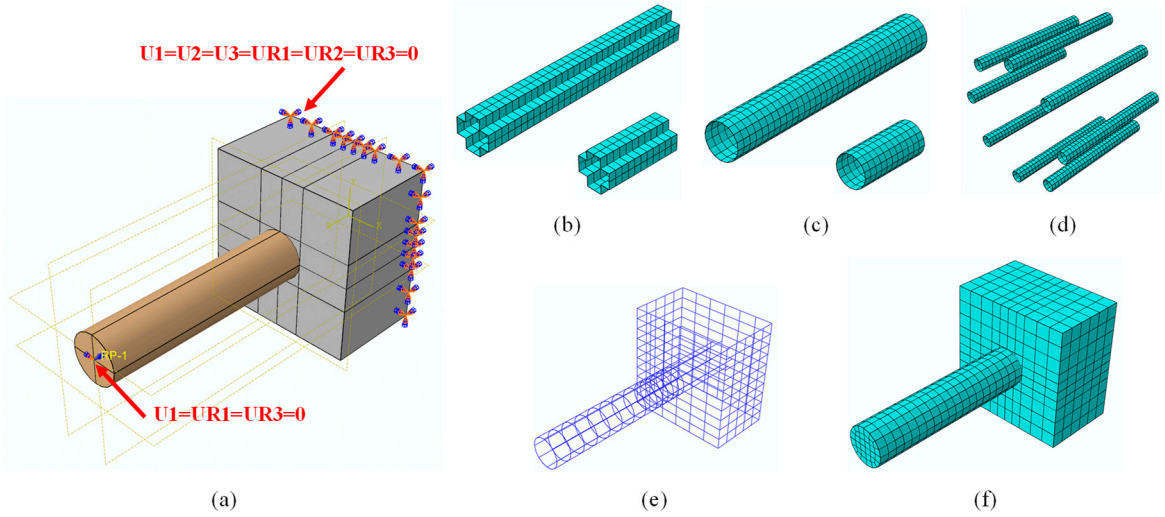

Figure 15. Schematic diagram of finite element model. (**a**) Boundary condition; (**b**) cross; (**c**) circular; (**d**) grouting sleeves; (**e**) reinforcement; (**f**) concrete mesh.

Table 5. Parameters for concrete plastic damage control.

Material	ψ	ε	f_{b0}/f_{c0}	K	ω
Concrete	30	0.1	1.14	0.6667	0.05

The "tie" constraint is employed between the pier shaft and the surface of the ground beam of the CIP specimen. In contrast, the "hard" contact is utilized between the pier shaft and the surface of the ground beam of the GY and GS specimens. Specifically, the "hard" contact is applied in the normal direction, while the "penalty" function Coulomb friction model with a friction coefficient of 0.5 is employed in the tangent direction. The steel reinforcement bars are embedded within the concrete, and "tie" constraints are employed to connect the steel tube of the ground beam to the steel tube of the pier shaft. Constraining the six degrees of freedom at the base of the bridge pier is a more appropriate approach to replicate the constrained conditions of the test specimen.

4.3. Calculation Results

Figure 16 depicts a comparison between the horizontal load (P)–displacement (Δ) curves derived from finite element analysis and those obtained from experimental tests. Figure 17 shows a comparison of the skeleton curves. Discrepancies and inadequacies can be seen in the hysteretic curves when comparing the two sets of data. The primary factors contributing to these disparities are as follows. Firstly, errors in specimen processing and test loading have resulted in asymmetric hysteretic curves, with the finite element analysis unable to account for these discrepancies, leading to a disparity between the positive and negative sides of the curves. Secondly, there might be a minor displacement between the reinforcement bars and the concrete of the actual specimen during loading, leading to a pinch effect in the hysteretic curve. However, the finite element calculation does not fully account for the initial defects caused by the embedded restraining method of the reinforcement bars, resulting in a slightly inflated curve in the finite element calculation. The hysteretic curves calculated from the finite element analysis closely match the test curves, and the main load characteristic points are close to the test results. As can be seen from the failure modes in Figure 18 (The red area in the figure indicates the damage location of the bridge pier), this observation validates the proposed finite element modeling method in this paper and offers valuable insights for subsequent engineering applications.

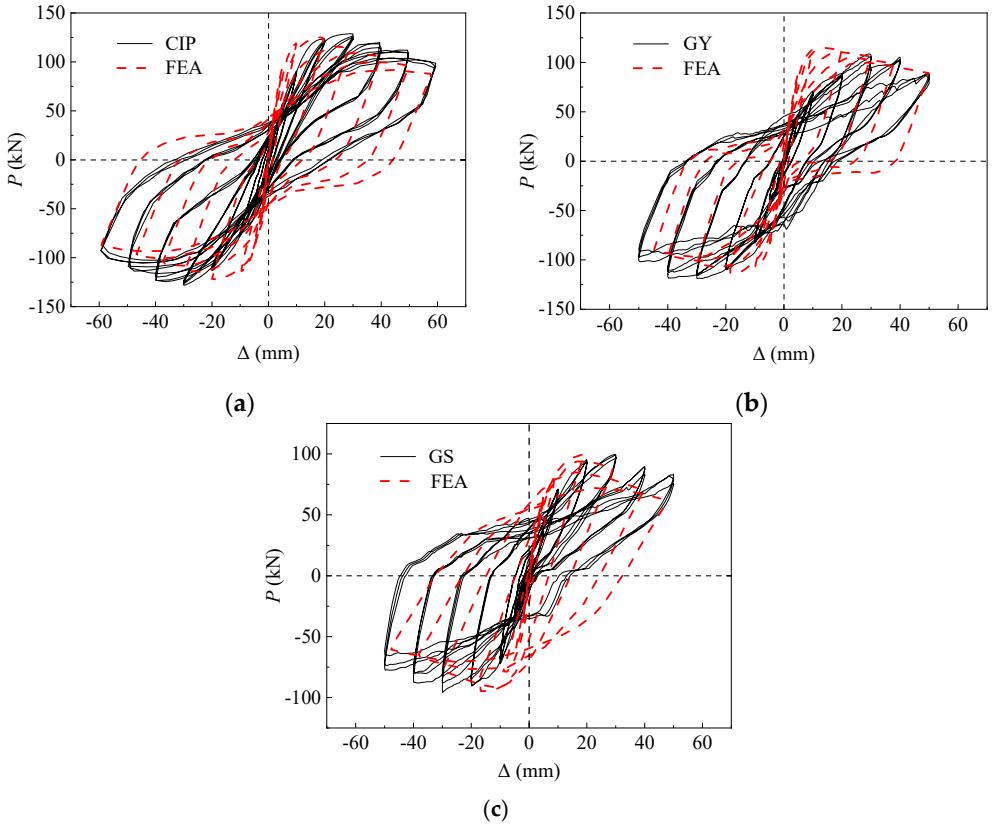

Figure 16. Comparison analysis of load–displacement curves. (**a**) CIP specimen; (**b**) GY specimen; (**c**) GS specimen.

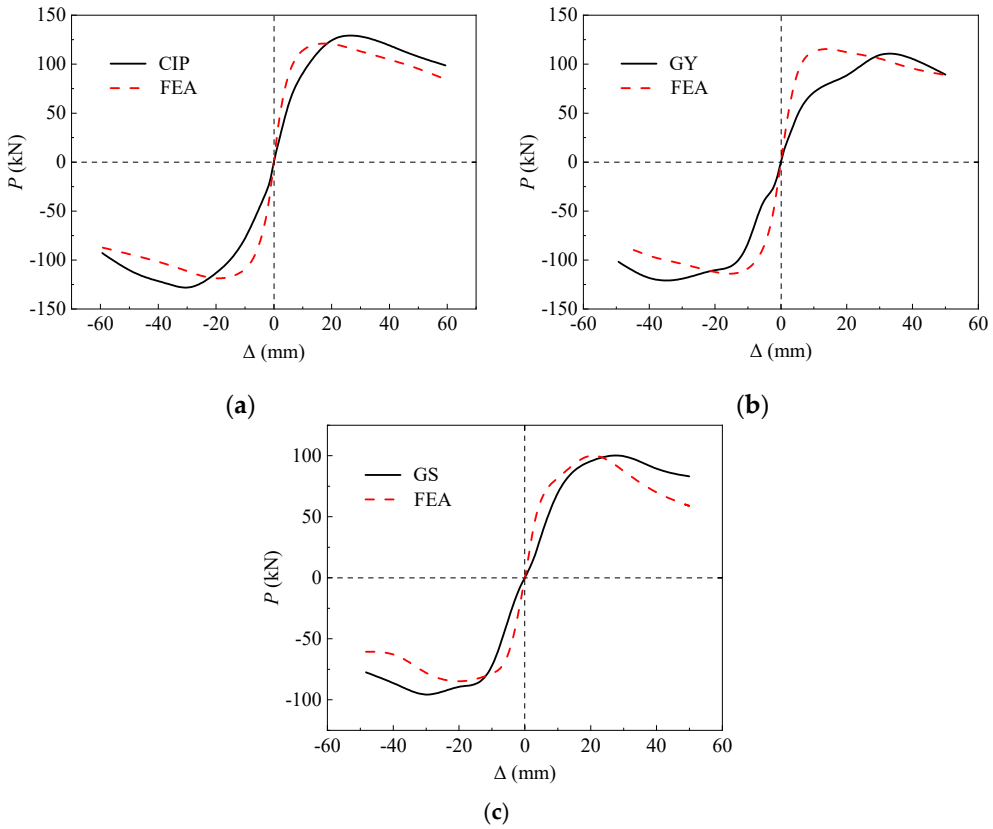

Figure 17. Comparison of skeleton curves. (**a**) CIP specimen; (**b**) GY specimen; (**c**) GS specimen.

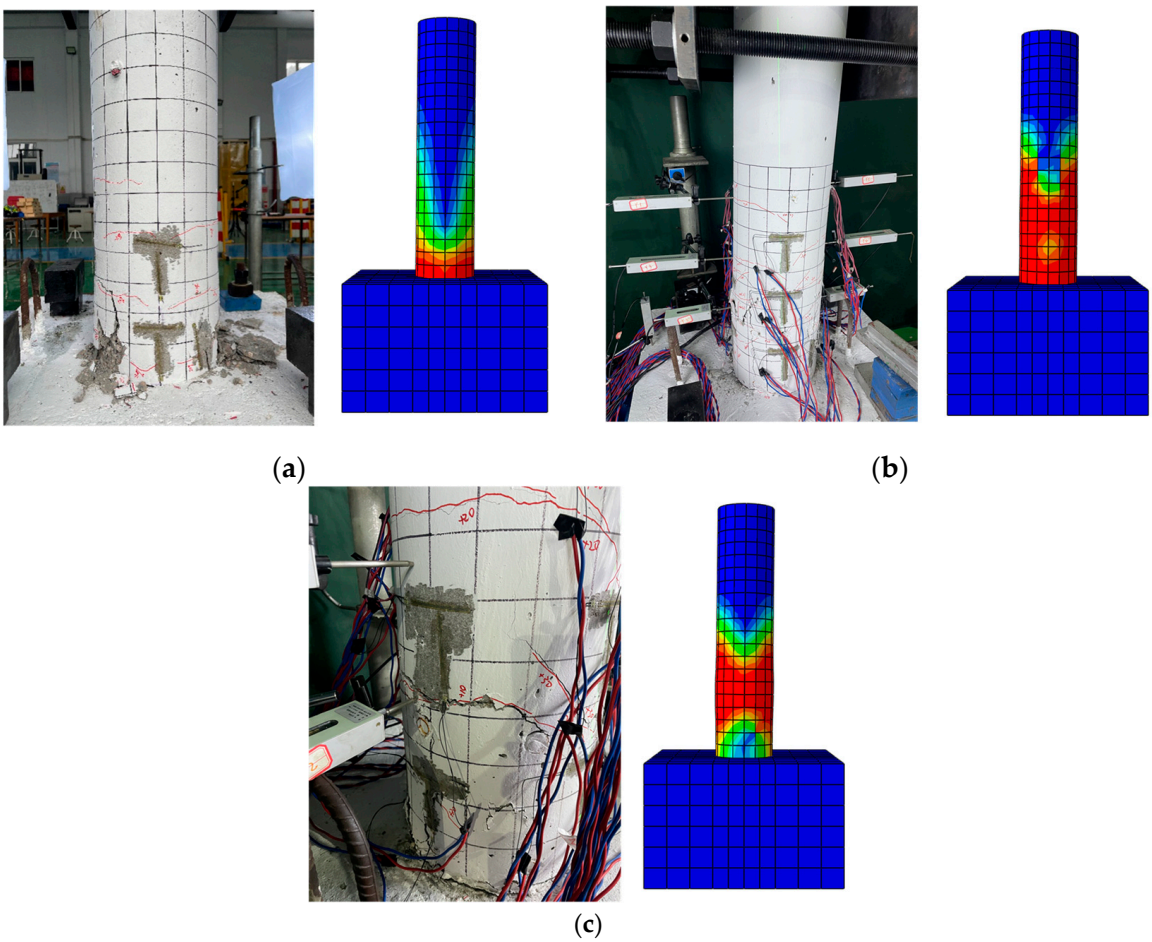

Figure 18. Comparison of failure modes. (**a**) CIP specimen; (**b**) GY specimen; (**c**) GS specimen.

5. Conclusions

This study proposes a design for a precast concrete bridge pier structure with a hybrid joint connection. Scaled-down specimens were created to investigate the seismic behavior of these precast concrete bridge piers, we compared the results of quasi-static tests on CIP specimens and precast specimens, and we examined the resulting damage phenomenon. The finite element model was ultimately established using ABAQUS software (ver. 6.14-4), and the principal findings are outlined as follows:

(1) All three specimens exhibited typical compression bending damage, with the CIP pier showing evident spalling of concrete cover in the plastic hinge region and deformation of reinforcing bars. This was attributed to the presence of a built-in steel tube shear key in the precast concrete bridge piers, resulting in an upward shift of the plastic hinge region. Consequently, cracks predominantly appeared on the upper side of the grouting sleeve and steel tube shear key, with no apparent spalling of concrete.

(2) The hysteretic curves of the specimens exhibited bow-shaped characteristics and generally appeared fuller, indicating a high energy dissipation capacity. Further examination of the hysteretic curves and skeleton curves indicated that the lateral bearing capacity of the precast bridge pier was marginally lower than that of the CIP pier, showing a decrease of 11.4%~23.9%. However, it was essentially similar to the CIP bridge pier in terms of ductility.

(3) The precast concrete bridge pier with a circular steel tube shear key showed a 16.4% increase in bearing capacity and a 19.0% increase in cumulative energy consumption, compared to those with a cross-shaped steel tube shear key. In general, the precast concrete bridge pier with a circular steel tube shear key exhibited good seismic behavior, essentially on par with the CIP pier.

(4) A refined model of the precast concrete bridge pier with hybrid joints was established in ABAQUS, based on the plane section assumption and a reasonable material constitutive model. The finite element analysis results exhibited strong concordance with the experimental data, with the primary load points closely aligning with the test values. This validates the precision of the numerical modeling approach outlined in this study, rendering it a valuable resource for future engineering applications.

Author Contributions: R.Z.: Investigation, Writing—Original Draft; L.Z.: Validation; H.Z.: Funding Acquisition, Writing—Review and Editing; S.Q.: Supervision. All authors have read and agreed to the published version of the manuscript.

Funding: This research was supported by the Natural Science Foundation of Fujian Province of China (Grant No. 2022J05099/2023J011035) and the Scientific Research Starting Foundation of Sanming University (Grant No. 21YG02).

Data Availability Statement: The data that support the findings of this study are available from the corresponding author on reasonable request.

Acknowledgments: The authors grateful acknowledge the Key Laboratory of Intelligent Construction and Monitoring of Engineering Structures in Fujian Province College, and the Key Laboratory of Engineering Material & Structure Reinforcement in Fujian Province College for their support with the experiments.

Conflicts of Interest: Author Liqun Zheng was employed by the company FuJian No.1 Construction Group Co., Ltd. The remaining authors declare that the research was conducted in the absence of any commercial or financial relationships that could be construed as a potential conflict of interest.

References

1. Mehrsoroush, A.; Saiidi, M.; Ryan, K. Development of Earthquake-Resistant Precast Pier Systems for Accelerated Bridge Construction in Nevada. Nevada Department of Transportation, 2017. Available online: https://rosap.ntl.bts.gov/view/dot/39296 (accessed on 1 June 2017).
2. Zhang, G.; Su, S.; Han, Q.; Xu, K.; Li, Z.; Du, X. Experimental and numerical investigation of seismic performance of prefabricated double-column piers used in accelerated bridge construction. *Eng. Struct.* **2023**, *293*, 116688. [CrossRef]
3. Han, Q.; Li, X.; Xu, K.; Lu, Y.; Du, X.; Wang, Z. Shear strength and cracking mechanism of precast bridge columns with grouted sleeve connections. *Eng. Struct.* **2021**, *230*, 111616. [CrossRef]
4. Guan, D.; Xu, R.; Yang, S.; Chen, Z.; Guo, Z. Development and seismic behavior of a novel UHPC-shell strengthened prefabricated concrete column. *J. Build. Eng.* **2022**, *46*, 103672. [CrossRef]
5. Witcher, T. Lake Pontchartrain Causeway. *Civ. Eng. Mag.* **2017**, *87*, 42–45. [CrossRef]
6. Zhang, L.; Sun, L.; Shang, Z. Real-time reliability assessment based on acceleration monitoring for bridge. *Sci. China Technol. Sci.* **2016**, *59*, 1294–1304. [CrossRef]
7. Zhang, Y.; Zhai, Y. Improvements in seismic performance of prefabricated bridge piers. *J. Highw. Transp. Res. Dev. (Engl. Ed.)* **2018**, *12*, 43–50. [CrossRef]
8. Wang, Z.; Zhang, J.; Lv, H.; Yan, X.; Li, T.; Qu, H. Seismic performance of short precast bridge columns with grouted splice sleeve (GSS) connectors for shear study: Quasi-static cyclic test and analytical estimation. *Soil Dyn. Earthq. Eng.* **2023**, *165*, 107659. [CrossRef]
9. Sun, C.; Zhuang, M.; Wang, Z.; Chen, B.; Gao, L.; Qiao, Y.; Zhu, H.; Zhang, W.; Yang, J.; Yu, C. Experimental investigation on the seismic performance of prefabricated fiber-reinforced concrete beam-column joints using grouted sleeve connections. *Struct. Concr.* **2023**, *24*, 4702–4718. [CrossRef]
10. Zhang, Y.; Zhu, Y.; Chen, Q.; Huo, W.; Shao, X. Precast columns connected with grouted corrugated steel sleeves and UHPC tenon under combined bending and compression. *Eng. Struct.* **2021**, *235*, 112080. [CrossRef]
11. Jin, Z.; Chen, K.; Pei, S. Cyclic response of precast, hollow bridge columns with postpour section and socket connection. *J. Struct. Eng.* **2022**, *148*, 06021005. [CrossRef]
12. Zou, S.; Wenliuhan, H.; Liu, Y.; Yang, Z.; Zhang, C.; Yuan, L. Seismic isolation technology for prestressed segmental precast piers. *Soil Dyn. Earthq. Eng.* **2022**, *161*, 107362. [CrossRef]
13. Wang, Y.; Cheng, Z.; Li, S.; Wang, J.; Zhong, R.; Zeng, M.; Ming, F.; Cui, B. Effect of a novel joint connection of UHPC wet joint and tapered sleeve locking-type couplers on the lateral cyclic response of precast segmental railway bridge columns. *Eng. Struct.* **2023**, *289*, 116333. [CrossRef]
14. Zhao, Y.; Zhang, H.; Pan, Z.; Li, G. Mechanical behavior of grouted sleeve connection for rebars in precast concrete structures and reliability analysis considering the ratio of anchorage length to rebar diameter. *Case Stud. Constr. Mater.* **2024**, *20*, e02883. [CrossRef]

15. Yuan, W.; Zhong, H.; Dang, X.; Deng, X. Research progress on seismic performance of precast piers with different connection forms. *J. Southeast Univ. (Nat. Sci. Ed.)* **2022**, *52*, 609–622. [CrossRef]
16. Zou, S.; Wenliuhan, H.; Liu, Y.; Zhai, Z.; Zhang, C. Seismic performance of precast assemble bridge piers with hybrid connection. *Struct. Eng. Mech.* **2023**, *85*, 407–426. [CrossRef]
17. Wang, R.; Ma, B.; Chen, X. Seismic performance of pre-fabricated segmental bridge piers with grouted splice sleeve connections. *Eng. Struct.* **2021**, *229*, 111668. [CrossRef]
18. Xin, G.; Xu, W.; Wang, J.; Yan, X.; Chen, Y.; Yan, W.; Li, J. Seismic performance of fabricated concrete piers with grouted sleeve joints and bearing-capacity estimation method. *Structures* **2021**, *33*, 169–186. [CrossRef]
19. Wang, C.; Jia, Y.; Liang, D. Equivalent plastic hinge length of sleeve connected precast bridge piers. *Structures* **2023**, *57*, 105243. [CrossRef]
20. Liu, Y.; Li, X.; Zheng, X.; Song, Z. Experimental study on seismic response of precast bridge piers with double-grouted sleeve connections. *Eng. Struct.* **2020**, *221*, 111023. [CrossRef]
21. Wang, Z.; Zhang, P.; Zhang, J.; Li, T.; Yan, X.; Qu, H. Seismic performance comparison of precast bridge columns with different shear span-to-depth ratios and connection designs via quasi-static cyclic test. *J. Bridge Eng.* **2022**, *27*, 04022094. [CrossRef]
22. Kenarkoohi, M.; Hassan, M. Review of accelerated construction of bridge piers-methods and performance. *Adv. Bridge Eng.* **2024**, *5*, 3. [CrossRef]
23. Qu, H.; Fu, J.; Li, T.; Wu, C.; Sun, X.; Wei, H.; Wang, Z. Experimental and numerical assessment of precast bridge columns with different grouted splice sleeve coupler designs based on shake table test. *J. Bridge Eng.* **2021**, *26*, 04021055. [CrossRef]
24. Ding, M.; Xu, W.; Wang, J.; Chen, Y.; Du, X.; Fang, R. Seismic performance of prefabricated concrete columns with grouted sleeve connections, and a deformation-capacity estimation method. *J. Build. Eng.* **2022**, *55*, 104722. [CrossRef]
25. Lei, S.; Liu, L.; Wu, F.; Lin, W.; Peng, K.; Cao, J. Seismic performance of short precast columns with UHPC grouted sleeve connections: An experimental and numerical study. *Structures* **2023**, *55*, 427–440. [CrossRef]
26. Li, X.; Zhang, G.; Han, Q.; Zhou, J.; Liu, X.; Du, X. Mechanical behavior of splice joints for bridge columns connected by grouted sleeves. *Soil Dyn. Earthq. Eng.* **2023**, *173*, 108078. [CrossRef]
27. Huang, H.; Li, M.; Zhang, W.; Yuan, Y. Seismic behavior of a friction-type artificial plastic hinge for the precast beam–column connection. *Arch. Civ. Mech. Eng.* **2022**, *22*, 201. [CrossRef]
28. *GB 50936—2014*; Technical Code for Concrete Filled Steel Tubular Structures. Architecture & Building Press of China: Beijing, China, 2014.
29. *GB/T 50081—2019*; Standard for Test Method of Physical Mechanical Properties on Concrete. Architecture & Building Press of China: Beijing, China, 2019.
30. *GB/T 228.1—2010*; Metallic Materials-Tensile Testing-Part 1: Method of Test at Room Temperature. Standards Press of China: Beijing, China, 2010.
31. *GB 50011-2010*; Code for Seismic Design of Buildings. Architecture & Building Press of China: Beijing, China, 2016.
32. Xu, Q.; Liu, Y.; Wang, J. Seismic performance of cross-shaped partially encased steel–concrete composite columns: Experimental and Numerical investigations. *Buildings* **2024**, *14*, 1932. [CrossRef]
33. Su, H.; Yang, C.; Sun, C.; Hu, L.; Fan, W. Seismic performance of precast multi-segment columns with grouted sleeves: Experimental and numerical investigations. *Eng. Struct.* **2024**, *301*, 117239. [CrossRef]
34. Zhao, C.; Li, Y.; Lu, Q. Study on seismic performance of honeycomb stiffened rib shaped concrete filled steel tube columns. *Case Stud. Constr. Mater.* **2022**, *17*, e01534. [CrossRef]
35. Wang, J.; Zhu, Z.; Wang, K. Study on seismic behavior of cross-shaped-steel-reinforced RPC columns. *Buildings* **2024**, *14*, 2310. [CrossRef]
36. *GB 50010-2010*; Code for Design of Concrete Structures. Architecture & Building Press of China: Beijing, China, 2015.
37. Menegotto, M. Method of analysis for cyclically loaded R. C. plane frames including changes ingeometry and non-elastic behavior of elements under combined normal force and bending. In Proceedings of the IABSE Symposium on Resistance and Ultimate Deformability of Structures, Lisbon, Portugal, 13–14 September 1973; pp. 15–22. Available online: https://api.semanticscholar.org/CorpusID:201285327 (accessed on 10 September 2024).
38. Zhu, J.; Qin, Y.; Shi, T. Calculation method for flexural capacity of prestressed UHPC-NC composite beams. *J. Cent. South Univ. (Nat. Sci. Ed.)* **2022**, *53*, 3989–4000. [CrossRef]